Journal of Materials Chemistry C

ROYAL SOCIETY OF CHEMISTRY

PAPER

View Article Online
View Journal

Cite this: DOI: 10.1039/d6tc00570e

Red-to-NIR luminescent trinuclear gold(I) complexes with exceptionally wide liquid crystalline temperature range

Tamon Nakao,†[a] Abhilash Sahu, †[a] Kenta Yamaguchi,[a] Arushi Rawat,[a] Kosuke Kaneko,‡[a] Kohsuke Matsumoto, [a] Ganesan Prabusankar [b] and Osamu Tsutsumi *[ab]

Luminescent trinuclear Au(I) complexes integrated into liquid crystalline (LC) frameworks provide a promising platform for developing anisotropic and stimuli-responsive soft materials. However, simultaneously achieving LC phase stability over a wide temperature range and phosphorescence under ambient conditions remains a challenge. Herein, we employed a combined linker and side-chain engineering strategy to tune the LC behaviour and photophysical properties of pyrazole-based cyclic trinuclear Au(I) complexes. Structural modulation was achieved by introducing flexible alkyl side chains of varying length and branching through ester linkages. The structure–property relationships of the Au(I) complexes were systematically investigated in the context of functional soft material design. The alkyl substituents exerted a pronounced influence on thermal behaviour: alkyl chain branching effectively lowered the melting temperature, while incorporation of ester linkages raised the LC-to-isotropic transition temperature. As a result of this synergistic effect, the complex bearing the longest branched alkyl side chain exhibited an exceptionally wide LC temperature window spanning more than 300 °C. In the LC state, all complexes self-assembled into a hexagonal columnar mesophase and displayed aggregation-induced emission behaviour. Alkyl chain substitution did not significantly affect the emission wavelength and excited-state lifetime but markedly enhanced the thermodynamic stability of the complexes. Thus, thermal and LC properties are governed primarily by molecular design, whereas photoluminescence characteristics are dictated by the aggregate structure. These findings highlight linker and side-chain engineering as an effective strategy for independently modulating the liquid crystallinity, thermal stability, and luminescence of Au(I)-based soft luminescent materials.

Received 23rd February 2026,
Accepted 24th March 2026

DOI: 10.1039/d6tc00570e

rsc.li/materials-c

Introduction

Luminescent metal complexes are key components of emerging optoelectronic and photonic technologies, such as organic light-emitting diodes, chemical sensors, and stimuli-responsive materials.[1–6] Au(I) complexes, in particular, have drawn sustained interest because they can achieve efficient room-temperature phosphorescence (RTP) with the appropriate design.[7–11] This feature is enabled by aurophilic interactions, which significantly enhance spin–orbit coupling. Cyclic trinuclear Au(I) complexes are an especially attractive class of emitters because they can form excimer- or exciplex-like excited states.[12–16] This process is facilitated by close Au···Au contacts enforced by their cyclic architecture through d^{10}–d^{10} interactions, making their emission behaviour highly sensitive to subtle modifications of their aggregated structures.

Beyond isolated molecular behaviour, many cyclic trinuclear Au(I) complexes exhibit aggregation-induced emission (AIE), in which luminescence is markedly enhanced in the aggregated or solid state owing to restricted molecular motions that suppress nonradiative decay pathways.[17–22] This AIE behaviour, combined with strong spin–orbit coupling and aggregation-dependent packing motifs, renders trinuclear Au(I) complexes an attractive platform for developing RTP-active materials operable under ambient conditions.[23–25]

In photonic and optoelectronic applications, deep-red to early near-infrared (NIR) (~650–800 nm) emission offers advantages such as reduced light scattering, increased penetration depth, and minimised background interference.[26–30]

[a] Department of Applied Chemistry, Ritsumeikan University, 1–1–1 Nojihigashi, Kusatsu 525-8577, Japan. E-mail: tsutsumi@sk.ritsumei.ac.jp
[b] Department of Chemistry, Indian Institute of Technology Hyderabad, Kandi Telangana 502285, India
† These authors contributed equally to this work.
‡ Present address: College of Liberal Arts and Sciences, Kitasato University, 1-15-1 Kitasato, Sagamihara, Kanagawa, 228-8555 Japan.

Consequently, there is growing interest in red-to-NIR emissive materials, which present a practical balance between long-wavelength emission, high quantum efficiency, and environmental robustness.[31–33] Achieving long-wavelength emission from molecular and coordination-based luminophores under ambient conditions is of considerable interest for next-generation photonic materials.[34–36] However, developing purely NIR-emissive materials that simultaneously exhibit high photoluminescence quantum yields (Φ), operational stability at room temperature, and tolerance to molecular oxygen remains highly challenging.[37–39] For molecular and coordination-based luminophores, extending emission into the NIR region is often accompanied by pronounced nonradiative decay and strong quenching of triplet excited states under ambient conditions, which severely limit emission efficiency.[40,41] Thus, red-to-NIR emissive materials that operate efficiently at room temperature in air—particularly those exhibiting phosphorescence—remain scarce despite their technological relevance.[42,43]

In parallel, integrating emissive metal complexes into liquid crystalline (LC) frameworks is a promising strategy for creating aligned, anisotropic, and stimuli-responsive soft materials.[44–48] In particular, discotic LC phases offer long-range one-dimensional columnar stacking and polarised optical responses, features that are highly advantageous for photonic and optoelectronic applications.[49–51] While many alkyl- or alkoxy-substituted π-conjugated cyclic cores readily form columnar mesophases, achieving LC behaviour for cyclic Au(I) complexes is difficult owing to their rigid metal-centred architecture and limited structural flexibility, which often favour crystallisation or restrict mesophase formation to a narrow temperature range. Prior studies showed that minimal substitution on pyrazole ligands can stabilise the columnar LC phases of such systems, albeit under restricted conditions, such as elevated temperatures above 100 °C.[52–54] Furthermore, side-chain engineering—particularly the position and chemical nature of the substituents—was demonstrated to exert a decisive influence on LC phase behaviour, including mesophase stability, phase transition temperatures, and the emergence of helical or chiral LC structures.[55,56]

Herein, we employed linker and side-chain engineering to develop a new series of pyrazolate-bridged cyclic trinuclear Au(I) complexes that exhibit red-to-NIR phosphorescence under ambient conditions and mesophase formation over a wide temperature range (Fig. 1a). In contrast to previously reported analogues bearing directly attached alkyl chains, the ester-functionalised complexes exhibited a well-defined hexagonal columnar (Col_h) LC phase during both heating and cooling, indicative of enantiotropic LC behaviour. Incorporation of an ester group at the C4 position of the pyrazole units effectively modulated the molecular shape and introduced additional conformational flexibility, thereby reducing packing frustration and promoting LC phase formation with enhanced fluidity. Notably, the complex bearing branched 2-butyloctyl side chains (**DTE6-Hex**) displayed a room-temperature Col_h phase and retained intense red-to-NIR phosphorescence ($\lambda_{em} \approx 740$ nm) with a high Φ (0.36) under ambient conditions. Furthermore,

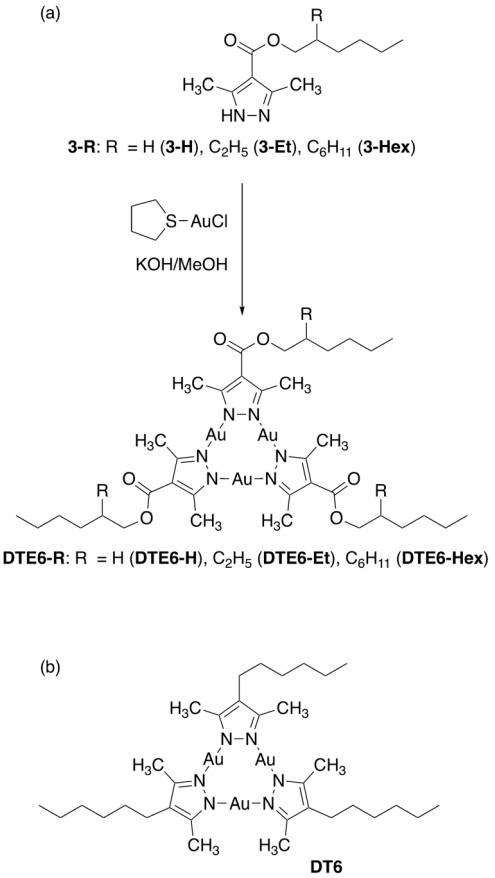

Fig. 1 (a) Synthetic route for cyclic trinuclear Au(I) complexes bearing alkyl side chains *via* ester linkages (DTE6-R). (b) Molecular structure of **DT6** as a reference cyclic trinuclear Au(I) complex.

this LC phase remained thermally stable up to the decomposition temperature (~300 °C), resulting in an exceptionally wide mesophase window exceeding 300 °C, which ranks among the broadest reported for luminescent LC materials.[57–59]

This work demonstrates that combined molecular engineering of the linker region and alkyl side chains, specifically through the introduction of ester linkages and systematic modulation of side-chain topology, enables simultaneous control over the LC phase behaviour and photophysical properties of cyclic trinuclear Au(I) complexes. In contrast to systems with directly attached alkyl chains, the ester-linked architecture provides a flexible structural platform that promotes liquid crystallinity, while side-chain branching plays a decisive role in realising room-temperature LC phases and tuning the mesophase temperature range. Importantly, the resulting complexes exhibit strong phosphorescence not only in the crystalline state but also within the LC phase, enabling polarised luminescence through controlled molecular orientation. These findings highlight the synergistic effect of linker and side-chain engineering as an effective design strategy for constructing room-temperature LC materials that combine AIE and RTP. More broadly, this work bridges luminescent molecular materials and soft photonic devices, opening new avenues for AIE- and RTP-active LC systems based on cyclic trinuclear Au(I) complexes.

Results and discussion

Synthesis and characterisation of Au(I) complexes

A new series of pyrazolate-bridged cyclic trinuclear Au(I) complexes bearing linear or branched alkyl side chains, denoted as DTE6-R, was synthesised following the synthetic route outlined in Fig. 1a. Detailed synthetic procedures and characterisation data for these complexes are provided in the Experimental section, while the synthesis of the pyrazole ligands is described in the SI. The previously reported **DT6** complex (Fig. 1b), bearing a directly attached *n*-hexyl chain, was examined as a reference to clarify the effects of linker and side-chain engineering on LC phase behaviour and photophysical properties.[18,21]

The DTE6-R complexes were obtained from the corresponding 3,5-dimethylpyrazole derivatives in moderate yield (26–61%) as a colourless solid or viscous material, depending on the side-chain structure. The complexes were characterised by ^{1}H and ^{13}C nuclear magnetic resonance (NMR) spectroscopy, Fourier-transform infrared (FTIR) spectroscopy, electrospray ionisation mass spectrometry (ESI-MS), and elemental analysis. The analytical data (see Experimental section and SI) are consistent with the proposed molecular structures.

In our previous study, single-crystal X-ray diffraction analysis revealed that **DT6** forms a ladder-like supramolecular polymer in the crystalline state through intermolecular Au···Au and Au···π interactions.[21] In contrast, suitable single crystals of the ester-functionalised DTE6-R complexes could not be obtained despite extensive crystallisation attempts, precluding detailed single-crystal structural analysis. Accordingly, their molecular packing and aggregation behaviour were evaluated using complementary bulk techniques, including differential scanning calorimetry (DSC) for phase transition analysis, polarised optical microscopy (POM) for mesophase identification, and powder X-ray diffraction (PXRD) for structural ordering, as discussed below.

Thermal behaviour of Au(I) complexes

To evaluate the thermal stability of the Au(I) complexes, thermogravimetric analysis (TGA) was performed in the temperature range of 25–600 °C at a heating rate of 5.0 °C min^{-1} (Fig. S8). The thermal decomposition temperature (T_{dec}), defined as the temperature corresponding to 5% weight loss, of each complex is listed in Table 1. The TGA thermograms further revealed residual ash contents of 54% for **DT6**, 47% for **DTE6-H**, 44% for **DTE6-Et**, and 39% for **DTE6-Hex**, which are in reasonable agreement with the theoretical Au contents calculated from their molecular formulas (52%, 47%, 43%, and 39%, respectively). These results support the compositional integrity of the synthesised complexes.

Notably, the T_{dec} values of the ester-functionalised DTE6-R complexes were higher than those of the reference complex **DT6**. Our previous study showed that the T_{dec} of mononuclear Au complexes correlates with the electronic characteristics of the ligand framework, with higher thermal stability observed for complexes bearing substituents with larger Hammett substituent constants (σ).[60] A similar correlation between σ and thermal stability is widely reported for various organic and organometallic systems.[61] In this context, the enhanced thermal stability of DTE6-R can be rationalised by the electron-withdrawing nature of the ester substituent (σ = 0.43 for $-COOCH_3$ *vs.* σ = −0.07 for $-CH_3$), which is consistent with the observed increase in T_{dec} relative to that of **DT6**.

To gain qualitative insight into the electronic effects of ester substitution and their possible relation to thermal stability, density functional theory (DFT) calculations were performed using DT1 and DTE1 as simplified models of **DT6** and DTE6-R, respectively (Fig. S21). The calculated molecular electrostatic potential maps (Fig. 2) indicated discernible differences in the electron density distribution around the Au centres depending on the substituent at the 4-position of the pyrazole ring. Introduction of the ester substituent led to a relative decrease in electron density at the Au centres, consistent with an increase in their cationic character. Although Mulliken atomic charges should be interpreted only qualitatively, the calculated charges of the Au atoms (1.83 for DT1 and 1.58 for DTE1) reflect the substituent-dependent electronic trend. Importantly, similar substituent-dependent electronic effects were observed in our previous work,[60] where the σ values of electron-withdrawing groups ($\sigma > 0$) were found to correlate with the thermal stability of related Au(I) complexes. The present results are therefore consistent with the previously established relationship between substituent electronic properties and thermal decomposition behaviour. In addition to the electronic effect of the ester linkage, the gradual decrease in thermal decomposition temperature observed from **DTE6-H** to **DTE6-Hex** can be attributed to the increasing steric bulk and flexibility of the

Table 1 Thermodynamic properties of Au(I) complexes[a]

Complex	Phase sequence and transition temperatures[b] (°C)		T_{dec} (°C)
DT6	Heating	Cr_1 94 (0.88) Cr_2 127 (1.5) Cr_3 140 (10) Col_h 144 (2.8) I	282
	Cooling	Cr_x 98 (−0.64) Cr_3 122 (−12) Col_h 141 (−4.5) I	
DTE6-H	Heating	Cr 132 (17) Col_{ho}[c]	302
	Cooling	Cr 121 (−18) Col_{ho}	
DTE6-Et	Heating	Cr_1 80 (1.1) Cr_2 99 (14) Col_h[c]	311
	Cooling	Cr_1 80 (−1.1) Cr_2 90 (−14) Col_h	
DTE6-Hex	Heating	S[d]–15 Col_{h1}[e] 35 (0.89) Col_{h2}[ce]	285
	Cooling	S_1 −38 (−0.10) S_2 −35 (−0.05) S_3 −20 (−0.03) S_4[d] −17 Col_{h1} 34 (−0.89) Col_{h2}	

[a] Abbreviations: Cr, crystalline; S, solid; I, isotropic; Col_h, hexagonal columnar (disordered); Col_{ho}, ordered hexagonal columnar; T_{dec}, thermal decomposition temperature. [b] Enthalpy change (ΔH, kJ mol^{-1}) for the phase transition is given in parentheses. ΔH values and transition temperatures were determined by DSC during the 2nd scanning cycle. [c] The clearing temperature could not be determined because the complexes exhibited the mesophase until T_{dec}. [d] Glass-like solid state retaining long-range hexagonal columnar order but lacking 3D crystallinity. [e] Col_{h1} and Col_{h2} are disordered hexagonal columnar mesophases with different degrees of short-range packing correlations. Col_{h1} contains localised, partially immobilised alkyl chain domains, whereas in Col_{h2}, these local correlations are fully relaxed, leaving only liquid-like correlations.

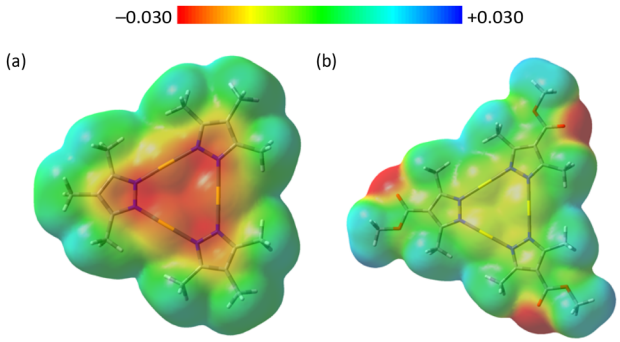

Fig. 2 Molecular electrostatic potential maps of (a) DT1 and (b) DTE1 as simplified models of **DT6** and DTE6-R, respectively. The electron density isosurface value is 0.0004 a.u., and the colour scale representing the relative electrostatic potential (negative to positive) is shown at the top. Atom colours: grey, C; white, H; blue, N; red, O; yellow, Au.

branched side chains. Bulkier substituents reduce intermolecular packing efficiency and weaken cohesive interactions in the condensed phase, resulting in slightly reduced thermal stability. Such packing effects have also been reported in alkyl-substituted liquid-crystalline systems.[62] Overall, the thermal decomposition behaviour of the present system is likely governed by multiple factors, including ligand electronic effects, side-chain structure, and the condensed-phase packing environment. Within this context, the observed increase in T_{dec} upon ester substitution is consistent with previously established electronic trends, suggesting that modulation of the electron density at the Au centres contributes, at least in part, to the enhanced thermochemical stability of the cyclic trinuclear Au(I) complexes.

The thermal phase transition behaviour of the Au(I) complexes was investigated by POM and DSC, and the corresponding data are summarised in Table 1. Representative DSC thermograms and optical textures observed in the LC phase are shown in Fig. 3. Trinuclear Au(I) complexes bearing 4-alkylpyrazole ligands are known to exhibit columnar LC behaviour.[49] For **DT6**, the DSC thermogram recorded during heating showed two relatively large endothermic peaks at 140 and 144 °C and several minor thermal features below 140 °C. The latter are attributed to crystal–crystal phase transitions, which reflect the polymorphism of **DT6** in the crystalline state. Between the two major endothermic events at 140 and 144 °C, the POM images revealed a dendritic texture characteristic of a Col_h LC phase. The combined DSC and POM results indicate that **DT6** exhibits an enantiotropic Col_h phase, consistent with an earlier report.[49]

In contrast, the DSC thermograms of **DTE6-H** and **DTE6-Et** displayed a single dominant thermal event during both heating and cooling cycles, although additional minor features were discernible for **DTE6-Et**. Above the main thermal transition, schlieren-like optical textures—also characteristic of the Col_h phase—were observed by POM. The appearance of these textures confirms the formation of the Col_h mesophase and indicates enantiotropic LC behaviour for both complexes. Compared with **DT6**, **DTE6-H** and **DTE6-Et** had significantly reduced crystalline-to-LC phase transition temperatures because

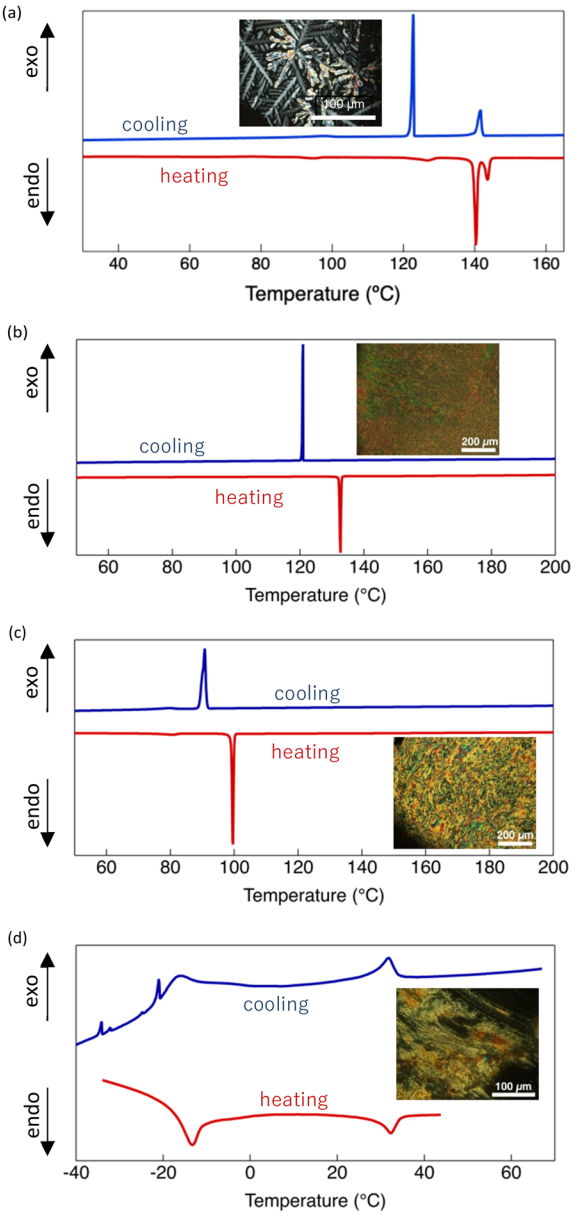

Fig. 3 DSC thermograms of (a) **DT6**, (b) **DTE6-H**, (c) **DTE6-Et**, and (d) **DTE6-Hex** (red: second heating; blue: second cooling). The scanning rate was 2 °C min^{-1}. Inset: POM images of the Au(I) complexes in the liquid crystalline phase: (a) **DT6** at 140 °C (cooling), (b) **DTE6-H** at 200 °C (heating), (c) **DTE6-Et** at 105 °C (heating), and (d) **DTE6-Hex** at room temperature (22 °C, heating).

of steric perturbation and increased conformational flexibility introduced by the ester linkage.

Notably, the DSC thermogram of **DTE6-Hex** exhibited a thermal event at −15 °C (Fig. 3d), whose broad shape suggests overlapping melting/freezing and glass-transition-like processes. Above this temperature, **DTE6-Hex** displayed macroscopic fluidity with schlieren-like optical textures characteristic of the Col_h phase, as confirmed by POM (Fig. 3d inset and Fig. S9). Another DSC feature appeared at approximately 35 °C, although no discernible change in optical texture or macroscopic fluidity was detected (Fig. S9). These combined observations suggest

that **DTE6-Hex** maintains a Col_h phase continuously from −15 °C up to its T_{dec}. A series of weak thermal events were additionally observed below –20 °C during cooling. Given their small enthalpy changes and the absence of corresponding features during heating, these transitions are tentatively attributed to local conformational relaxation of the ester-linked branched alkyl side chains within the condensed phase, rather than changes in long-range molecular packing. Importantly, for all ester-functionalised DTE6-R complexes, no Col_h–isotropic phase transition was detected prior to thermal decomposition. Consequently, exceptionally wide temperature ranges of Col_h phase stability were achieved, spanning approximately 170 °C for **DTE6-H**, 212 °C for **DTE6-Et**, and 300 °C for **DTE6-Hex**. In this work, the LC temperature window is defined as the temperature interval between the melting transition and T_{dec}, determined at 5% weight loss in TGA. The LC temperature window observed for **DTE6-Hex** (∼300 °C) is among the widest reported for luminescent metallomesogens. Representative cyclic trinuclear Au(I) complexes and related metallomesogenic systems reported in the literature typically exhibit mesophase windows below ∼150 °C.[45,52,58] Minor DSC features observed at approximately 80 °C for **DTE6-Et** and −20, −35, and −38 °C for **DTE6-Hex** are tentatively attributed to local crystallisation or glass transition processes of the alkyl side chains, although their precise origin cannot be unambiguously assigned on the basis of the present data.

Comparison of melting behaviour revealed that ester-functionalised DTE6-R exhibited much lower melting temperatures than **DT6**, which bears directly attached alkyl chains. While the introduction of the ester linkage perturbs efficient crystalline packing by increasing conformational flexibility at the linker region, the magnitude of melting point depression is strongly dependent on the side-chain architecture. In particular, branched alkyl substituents noticeably reduce the melting temperature, indicating that steric bulk and conformational disorder associated with branching play a dominant role in suppressing crystallisation. This interpretation is further supported by the difficulty in obtaining single crystals of sufficient quality for structural analysis from the ester-functionalised complexes, especially those bearing branched side chains.

In contrast to melting behaviour, the upper temperature limit of the LC phase increased substantially upon introduction of the ester linkage. For all DTE6-R complexes, the Col_h phase persisted up to the T_{dec} without an intervening isotropic phase. This decoupling of melting point depression and LC phase stabilisation highlights the distinct yet complementary roles of side-chain branching and ester linkage: the former effectively suppresses crystallisation at low temperatures, while the latter significantly stabilises the columnar LC phase at elevated temperatures. Thus, the exceptionally wide LC temperature window of DTE6-R arises from the synergistic combination of ester linker incorporation and branched side-chain engineering, which independently define the lower and upper thermal boundaries of the LC phase.

To establish a direct structure–property correlation for the phase transitions observed by DSC and POM, variable-temperature powder X-ray diffraction (VT-PXRD) measurements were performed (Fig. 4). All diffraction angles (2θ) were converted to interplanar distances (d) using Bragg's law, and the resulting data are summarised in Table 2. In VT-PXRD measurements, numerous sharp reflections typically characterise a crystalline phase, whereas a limited number of reflections in the small-angle region, accompanied by a diffuse halo in the wide-angle region, generally indicates a LC state. As shown in Fig. 4a, **DT6** exhibited a diffraction pattern characteristic of a crystalline phase up to approximately 130 °C. Above this temperature, the diffraction profile changed noticeably, and three reflections appeared in the small-angle region with d-spacings of 14.9, 8.7, and 7.5 Å. These reflections can be indexed to the (100), (110), and (200) planes of a two-dimensional (2D) hexagonal lattice, respectively, based on their characteristic spacing relationship. Concomitantly, a broad halo emerged in the wide-angle region, which is consistent with the formation of an LC phase at 140 °C. Upon further heating to 150 °C, the diffraction profile became essentially featureless within the measured 2θ range, indicating the loss of long-range positional order and consistent with a transition to an isotropic liquid state. Taken together with the DSC and POM results, the diffraction features observed in the intermediate temperature range are therefore consistent with the formation of a Col_h mesophase for **DT6**.

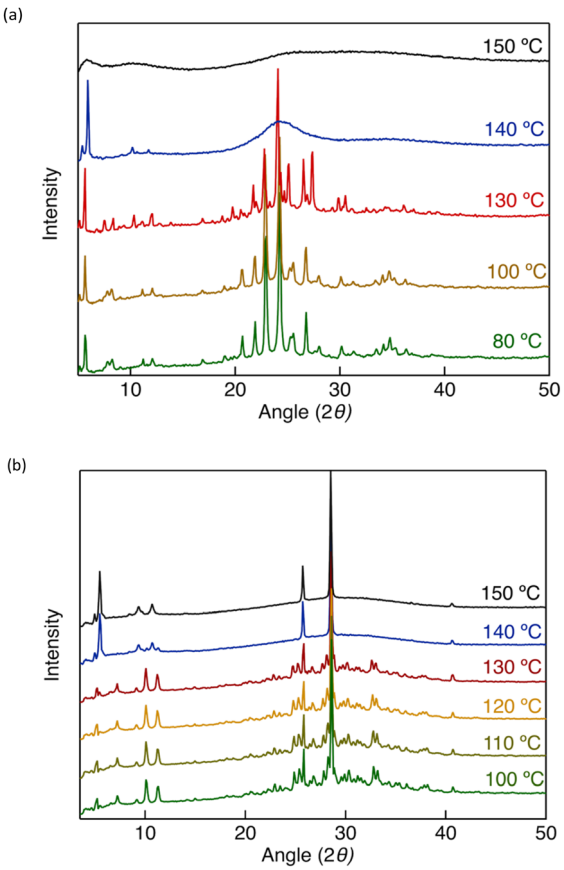

Fig. 4 PXRD patterns of (a) **DT6** and (b) **DTE6-H** as a representative example at different temperatures.

Table 2 PXRD data for **DT6**, **DTE6-H**, and **DTE6-Et** in the liquid crystalline temperature range

Complex	d (Å)	Index (hkl)	a_h[a] (Å)
DT6 (140 °C)	14.9	(100)	17.2
	8.7	(110)	
	7.5	(200)	
DTE6-H (150 °C)	15.9	(100)	18.4
	9.3	(110)	
	8.1	(200)	
DTE6-Et (100 °C)	17.2	(100)	19.9
	9.7	(110)	
	8.7	(200)	
DTE6-Hex (23 °C)	18.8	(100)	21.7
	10.7	(110)	
	9.7	(200)	
	7.4	(210)	
	6.5	(300)	

[a] Calculated assuming a 2D hexagonal lattice: $a_h = (2/\sqrt{3})d_{100}$.

In this context, it is instructive to consider the molecular packing within the Col_h mesophase of **DT6**. The previously reported single-crystal X-ray structure of **DT6** revealed hexyl side chains folded along the columnar axis in the crystalline state (Fig. S12). From the crystal structure, the centroid of the rigid core unit—defined as the geometric centre of the three Au atoms bridged by pyrazolate ligands (indicated by the red point in Fig. S12)—was identified. The distance from this centroid to the carbon atom of the side chain attached to the 4-position of the pyrazole ring is approximately 6.4 Å. From this value, the diameter of the rigid core unit is estimated to be ~13 Å. DFT calculations further indicated that the distance between the terminal carbon atoms of the optimised hexyl side chain fragment is also approximately 6.4 Å. If the side chains extend laterally without folding, then the effective molecular diameter of **DT6**, when approximated as a disc-like unit, is 26 Å. However, the lattice parameter a_h determined from PXRD measurements is only 17.2 Å, indicating that the intercolumnar distance in the Col_h phase is substantially smaller than the estimated molecular diameter. Although a definitive structural model cannot be established based solely on PXRD data, this discrepancy suggests that, even in the Col_h mesophase, the alkyl side chains do not extend fully in the radial direction. Instead, they are likely folded along the columnar axis and/or interdigitated between neighbouring columns, thereby enabling dense columnar packing. Such packing behaviour is consistent with the formation of a compact hexagonal columnar arrangement despite the presence of flexible alkyl substituents.

An analogous analysis of diffraction features was performed for DTE6-R (Fig. 4b and Fig. S10). For **DTE6-H**, multiple sharp Bragg reflections were observed at 120 °C, indicating a crystalline state. Upon heating to 150 °C, the diffraction profile changed markedly, and three sharp reflections appeared in the small-angle region with d-spacings of 15.9, 9.3, and 8.1 Å, which can be indexed to the (100), (110), and (200) planes, respectively. Importantly, the small-angle reflections obeyed the characteristic spacing ratio of $1:1/\sqrt{3}:1/2$, consistent with a 2D hexagonal lattice with $p6mm$ symmetry. Taken together with the DSC and POM results, these diffraction features support the formation of a Col_h mesophase for **DTE6-H**. Concomitantly, a broad halo emerged in the wide-angle region, which is commonly associated with the increased conformational and dynamic disorder of flexible alkyl chains and consistent with a crystalline-to-LC phase transition. Notably, in addition to the diffuse halo, two reproducible and relatively sharp features were observed in the wide-angle region (2θ = 28.6 and 25.7°), corresponding to d-spacings of approximately 3.1 and 3.4 Å. The persistence of these features in the Col_h phase indicates the presence of pronounced short-range intracolumnar correlations within the columnar stacks. Such distances are characteristic of intermolecular packing along the columnar axis and frequently observed in ordered Col_h systems.[63,64] While interactions involving Au centres and ligand π-systems may contribute to the emergence of these short-range correlations, the coexistence of two distinct d-spacings suggests the presence of multiple local packing motifs within the columns. On this basis, the LC phase of **DTE6-H** is assigned as an ordered Col_{ho} phase, characterised by well-developed intracolumnar short-range order. A more specific assignment of the underlying intermolecular interactions, however, cannot be made solely on the basis of PXRD data.

In contrast to **DTE6-H**, **DTE6-Et** showed a comparatively straightforward diffraction behaviour (Fig. S10a). Above the phase transition temperature, three sharp reflections emerged in the small-angle region, indicating the formation of a Col_h phase. The corresponding d-spacing ratio was consistent with that expected for a 2D hexagonal lattice with $p6mm$ symmetry. In the wide-angle region, the diffraction pattern was dominated by a broad halo, and no well-defined sharp reflections were observed. Accordingly, the mesophase of **DTE6-Et** can be classified as a disordered Col_h phase.

For **DTE6-Hex**, the thermal event observed at −15 °C corresponds to fusion or melting and could be readily identified by POM (Fig. S9). In contrast, the thermal feature detected at 35 °C could not be clearly distinguished by POM because of the similar optical textures and macroscopic fluidity of the two phases. To clarify the structural origin of these thermal events, VT-PXRD measurements were initially performed (Fig. S10b). At room temperature (23 °C), the PXRD pattern of **DTE6-Hex** exhibited several intense and sharp reflections in the small-angle region. These reflections can be indexed to the (100), (110), (200), and (210) planes of a 2D hexagonal lattice, confirming the formation of a Col_h mesophase. In addition to the small-angle reflections, a weak and broad halo was observed in the wide-angle region (2θ = 26.9°), indicating the absence of long-lived crystalline packing at the molecular level. Above 35 °C, the overall PXRD profile remained essentially unchanged, demonstrating that the hexagonal columnar arrangement is preserved in terms of long-range positional order.

Because the thermal feature at 35 °C could not be unambiguously resolved by either POM or PXRD alone, small-angle X-ray scattering (SAXS) measurements were subsequently employed

to probe more subtle changes in internal order (Fig. S11). At temperatures below −15 °C, the SAXS profile of **DTE6-Hex** exhibited four sharp reflections in the small-angle region, indicative of well-defined long-range positional order associated with a 2D hexagonal columnar lattice. In contrast, the wide-angle region displayed a complex superposition of scattering features, including broad halos centred at q = 13–15 and ∼20 nm^{-1}, several weak but discernible sharp peaks, and an additional broad feature at approximately q = 18 nm^{-1}. These q values correspond to real-space distances of approximately 3–5 Å, which are characteristic of short-range intermolecular correlations in the condensed phase. The coexistence of diffuse halos and weak, sharp features in the wide-angle region indicates that the low-temperature phase is not a simple, uniformly ordered molecular crystal. Rather, these features are best interpreted as correlation peaks arising from enhanced short-range positional correlations that persist over limited spatial extents without developing into full three-dimensional crystallinity. In this framework, the broad halos at q = 13–15 nm^{-1} are consistent with liquid-like correlations of flexible alkyl segments, whereas the superimposed weak sharp peaks reflect locally ordered packing motifs with finite correlation lengths. Such hierarchical ordering—long-range hexagonal positional order of the columns combined with heterogeneous, spatially confined local packing—is plausible for **DTE6-Hex** given the presence of bulky branched alkyl chains that hinder uniform crystallisation and promote partial ordering even in the low-temperature solid state.[65–67]

Above −15 °C (*e.g.*, 22 °C), the SAXS pattern retained both the sharp low-q reflections arising from the hexagonal columnar lattice and wide-angle features, including diffuse halos and weak correlation peaks. Importantly, the intensities of the weak sharp peaks decreased progressively with increasing temperature and became barely discernible at 22 °C. This behaviour indicates that the long-range positional order of the columnar lattice is preserved throughout the temperature range from −15 to 35 °C, whereas short-range packing correlations on the angstrom length scale are gradually weakened by thermal activation. A consistent structural interpretation for this intermediate regime is a disordered Col_{h1} phase, in which the columns remain well organised, whereas locally correlated packing motifs—primarily associated with partially immobilised branched alkyl segments—persist only over limited length scales.[63,64,68] These motifs give rise to temperature-sensitive correlation peaks rather than true Bragg reflections and progressively lose coherence upon heating. Alternative descriptions in terms of finite-length intracolumnar correlations or glassy side-chain freezing are also compatible with the present scattering data.

Upon further heating above 35 °C, the weak sharp features in the wide-angle region disappeared completely, whereas the diffuse halos and broad feature centred at q = 18 nm^{-1} remained essentially unchanged. At the same time, the well-defined small-angle reflections associated with the hexagonal columnar lattice persisted without appreciable changes in position or intensity. At 40 °C, four sharp reflections were clearly observed in the small-angle region, with q-values following the characteristic ratio of $1:\sqrt{3}:2:\sqrt{7}$. These reflections can be unambiguously indexed to the (100), (110), (200), and (210) planes of a 2D hexagonal lattice, from which the lattice parameter a_h is estimated to be approximately 23 Å (Table S2). The absence of sharp wide-angle reflections at this temperature, together with the persistence of diffuse halos, indicates that intracolumnar packing lacks long-lived short-range order and is dominated by dynamically averaged, liquid-like correlations. Accordingly, the high-temperature phase above 35 °C is assigned to a fully disordered Col_{h2} phase, in which the hexagonal arrangement of columns is robust, whereas localised packing motifs responsible for the correlation peaks at lower temperatures are completely melted or lose coherence.

The phase behaviour of **DTE6-Hex** can be interpreted as a hierarchical ordering process involving progressively increasing intracolumnar disorder. At low temperature (<−15 °C), the material exists in a glass-like solid state that retains long-range hexagonal columnar positional order but lacks three-dimensional crystallinity. Upon heating, this state transforms into two distinct hexagonal columnar mesophases, designated Col_{h1} and Col_{h2}, distinguished based on combined PXRD, SAXS, DSC, and POM data. In the Col_{h1} phase, the SAXS pattern exhibits well-defined hexagonal reflections alongside weak wide-angle scattering features, indicative of partial local packing order within the columns. On further heating to the Col_{h2} phase, these wide-angle features disappear while the hexagonal columnar reflections are retained, signalling a reduction in local molecular packing order with preservation of the long-range columnar lattice. This structural change is accompanied by a subtle thermal transition observed in the DSC trace (Fig. S13).

The thermal event at –15 °C is accordingly assigned to a transition from a partially ordered LC-like solid—characterised by frozen hexagonal columnar positional order with heterogeneous short-range packing—to the Col_{h1} mesophase, which retains residual local correlations. The feature at 35 °C corresponds to a further disordering process within the columnar phase, involving relaxation of locally ordered alkyl-chain domains, leading to the more disordered Col_{h2} state. A comparable hierarchy of intracolumnar ordering has been reported for discotic perylene bisimide assemblies bearing branched alkyl side chain,[69] in which a low-order hexagonal columnar phase with short-range intracolumnar correlations coexists with a higher-order columnar phase exhibiting well-defined molecular packing. Collectively, these findings demonstrate that side-chain architecture can decouple long-range columnar positional order from local molecular packing order.

Overall, the introduction of branched alkyl side chains considerably lowers the melting temperature while stabilising the hexagonal columnar mesophase across an exceptionally wide temperature range. This molecular design strategy enables a room-temperature Col_h mesophase with tuneable degrees of intracolumnar disorder and highlights the effectiveness of side-chain engineering in controlling hierarchical structural organisation in cyclic trinuclear Au(I) complexes.

Analogous to the case of **DT6**, the effective disc diameter estimated from the rigid core and ester-linked alkyl side chains of DTE6-R is substantially larger than the experimentally

determined lattice parameter a_h. This geometric mismatch indicates that, in the Col_h mesophase of DTE6-R, the flexible alkyl side chains do not extend radially but instead undergo interdigitation and/or folding along the columnar axis, thereby enabling dense columnar packing despite the presence of bulky substituents.

Photophysical properties of Au(I) complexes at room temperature

The photophysical properties of the Au(I) complexes were systematically investigated. Ultraviolet-visible (UV-vis) absorption spectra in dilute dichloromethane solution, together with photoluminescence and excitation spectra measured in the crystalline or Col_{h1} state, are shown for **DTE6-H** and **DTE6-Hex** as representative examples in Fig. 5. The absorption spectra exhibited intense bands exclusively in the UV region, with no detectable absorption in the visible region, indicating that the complexes are optically transparent in the visible range—an advantageous characteristic for luminescent materials.

All DTE6-R complexes showed an absorption maximum (λ_{max}^{abs}) at approximately 240 nm in dilute dichloromethane solution, and no significant shift in λ_{max}^{abs} was observed upon introduction of branched alkyl side chains (Fig. 5 and Fig. S14). To gain insight into the electronic origin of these absorption features, time-dependent density functional theory (TD-DFT) calculations were performed for the model complex DTE1. Major absorption bands were predicted in the range of 236–239 nm in the UV region (Table S4), and the calculated absorption energies were in good agreement with those derived from the experimentally λ_{max}^{abs} values. Analysis of the molecular orbitals involved in these transitions indicated that the absorption bands of DTE1 at 236–239 nm have mixed ligand-to-metal charge transfer and metal-centred character (Fig. S22). The corresponding TD-DFT results for the reference model DT1 are also summarised in Table S4.

None of the investigated complexes exhibited detectable photoluminescence in dilute solution within the sensitivity limits of the measurement. In contrast, intense luminescence was observed in the condensed phase at room temperature (25 °C) (Fig. 5 and Table 3). All complexes displayed emission in the NIR region, with the maximum centred at approximately 740–750 nm. Emission in the NIR region is advantageous for photonic and optoelectronic applications because of reduced optical scattering and deeper penetration of NIR light. Although **DTE6-H** and **DTE6-Hex** adopted different phases at 25 °C, their emission spectra were nearly identical, indicating a common emissive species in the condensed state. Our previous study demonstrated that the luminescence of **DT6** arises from aggregates formed *via* intermolecular Au···Au and Au···π interactions, resulting in a ladder-like supramolecular polymer.[21] Although single-crystal structural analysis of the DTE6-R complexes was not possible owing to their low crystallinity, the close similarity in emission wavelength and spectral shape to those of **DT6** strongly suggests that their luminescence likewise originates from aggregated species formed through analogous intermolecular interactions.

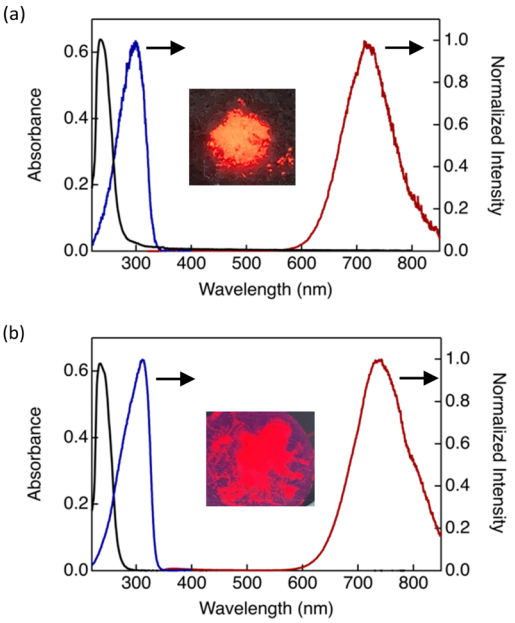

Fig. 5 Absorption and corrected photoluminescence spectra of (a) **DTE6-H** and (b) **DTE6-Hex** at 25 °C. Colour legends: black, absorption spectra in CH_2Cl_2 solution (1.0×10^{-5} mol L^{-1}); red, photoluminescence spectra (λ_{ex} = 300 nm) in the crystalline (Cr) (**DTE6-H**) or disordered hexagonal columnar (Col_{h1}) state (**DTE6-Hex**); blue, excitation spectra (λ_{em} = 725 nm) in the Cr (**DTE6-H**) or Col_{h1} state (**DTE6-Hex**). Inset: Photographs of the Au(I) complexes in the condensed phase at 25 °C under UV irradiation at 254 nm.

Table 3 Photophysical parameters of Au(I) complexes in the condensed phase at 25 °C in air

Complex	Phase[a]	λ_{max}^{em} [b] (nm)	Φ[bc]	τ (μs)	k_r [d] (s^{-1})	k_{nr} [d] (s^{-1})
DT6[21]	Cr	733	0.75	13	5.8×10^4	1.9×10^4
DTE6-H	Cr	721	0.86	14	6.1×10^4	1.0×10^4
DTE6-Et	Cr	731	0.49	15	3.3×10^4	3.4×10^4
DTE6-Hex	Col_h	741	0.36	14	2.6×10^4	4.6×10^4

[a] Abbreviations: Cr, crystalline; Col_h, hexagonal columnar (disordered). [b] The excitation wavelength for steady-state measurements was 280 nm. [c] The luminescence intensity was integrated from 600 to 850 nm to estimate Φ. [d] The rate constants for radiative transition (k_r) and non-radiative deactivation (k_{nr}) are equal to Φ/τ and $(1 - \Phi)/\tau$, respectively.

The gradual red shift in emission maxima from **DTE6-H** to **DTE6-Hex** is likely associated with subtle changes in intermolecular packing induced by the increasing steric bulk of the side chains. Such steric effects can influence Au···Au metallophilic interactions between neighbouring trinuclear units, thereby influencing the energy of the emissive excited state. Differences in condensed-phase structures may further contribute to this trend, as **DTE6-H** and **DTE6-Et** emit from crystalline phases, whereas **DTE6-Hex** exhibits the Col_h mesophase at room temperature. The distinct molecular organisation within these phases can give rise to slightly different intermolecular interactions and excited-state energies, thereby contributing to the observed bathochromic shift.

Consistent with this interpretation, the excitation spectra in the condensed phase differed considerably from the absorption

spectra in dilute solution (Fig. 5), reflecting the formation of aggregated emissive states in the condensed phase. To further verify this hypothesis, AIE behaviour was examined in mixed solvent systems composed of a good solvent (THF) and a poor solvent (water) with varying volume fractions (f_w) (Fig. 6 and Fig. S16). As a representative example, the AIE behaviour of **DTE6-Hex** is shown in Fig. 6. In pure THF, the complexes exhibited negligible emission. However, as f_w increased, the emission intensity rose gradually and then sharply once a threshold of approximately 20% was exceeded. This pronounced enhancement of luminescence is attributed to the onset of molecular aggregation induced by the poor solvent environment. These observations unambiguously confirm that the emission of the DTE6-R complexes is governed by an AIE mechanism and further support the notion that the emissive aggregates formed by these complexes are structurally analogous to those previously identified for **DT6**.

The emission spectra observed in THF/water mixtures display a partially resolved dual-band profile under AIE conditions (Fig. 6 and Fig. S16). Rather than representing a vibronic progression of a single emissive state, this behaviour is more plausibly attributed to heterogeneous aggregates with slightly different intermolecular Au···Au and Au···π interactions. Such variations in intermolecular interactions may generate closely spaced emissive excited states associated with metallophilically coupled Au(I) aggregates, giving rise to the observed dual-band emission. The spectral differences between THF/water mixtures and the condensed phases can be rationalised by differences in aggregate structure: aggregation under kinetically controlled conditions in THF/water mixtures may produce more disordered aggregates than those present in the solid and LC phases. Heterogeneous local environments within these aggregates may further contribute to the dual-band emission, as molecules residing in densely packed bulk regions and those near solvent-exposed surfaces may experience slightly different intermolecular interactions and local solvation conditions, leading to slightly different emissive energies.

To clarify the luminescence mechanism, the Φ and emission lifetimes (τ) of the complexes were measured in the condensed phase at room temperature in air (Table 3). All complexes exhibited a single-exponential decay profile monitored at 725 nm (Fig. 7 and Fig. S15). Notably, no significant differences in the decay profile or lifetime were observed among the different phase states. The emission lifetimes of all complexes fell in the microsecond timescale, indicating that the observed emission originates from RTP. In general, molecular systems rarely exhibit RTP with high Φ because the nonradiative decay pathways of long-lived triplet excited states are readily activated by thermal perturbations, such as internal molecular motions and collisional quenching. Nonradiative processes strongly compete with the inherently slow radiative transitions from triplet excited states. Moreover, triplet states are efficiently quenched by molecular oxygen under ambient conditions. In this context, the efficient RTP of the present Au(I) complexes is particularly notable and highlights their potential as robust RTP-active materials for optoelectronic and photonic applications.

Unlike τ, Φ showed a clear dependence on molecular structure. Because the photoluminescence of the complexes originates from aggregated states, the emission efficiency is expected to be governed not solely by the primary molecular structure but predominantly by the nature of the aggregated packing structure. This interpretation is further supported by

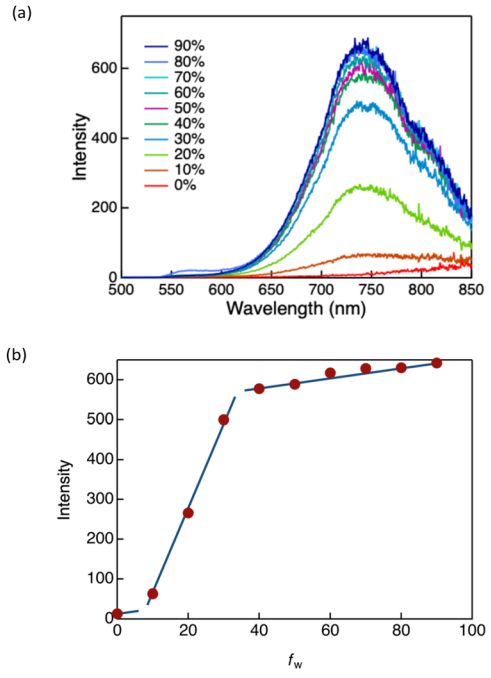

Fig. 6 (a) Photoluminescence spectra of **DTE6-Hex** (5.0×10^{-5} mol L^{-1}) in a THF/H_2O mixed solvent with varying H_2O fractions (f_w = 0–90%) (λ_{ex} = 300 nm). (b) Luminescence intensity of the solution at 750 nm as a function of f_w.

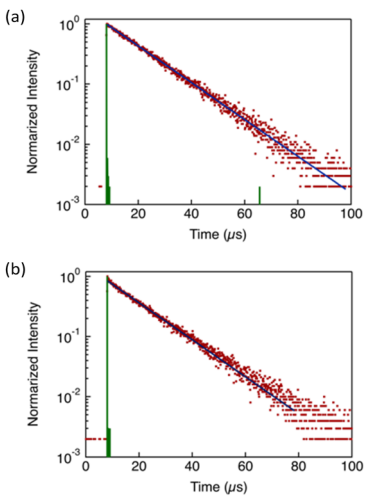

Fig. 7 Luminescence decay profiles of Au(I) complexes in the condensed phase at 25 °C in air: (a) **DTE6-H** in the crystalline phase and (b) **DTE6-Hex** in the disordered hexagonal columnar (Col_{h1}) phase (red, observed luminescence decay; blue, fitting curve; green, instrument response function). The decay upon excitation at 280 nm was monitored at 725 nm for **DTE6-H** and 740 nm for **DTE6-Hex**.

TD-DFT calculations and the absorption behaviour in dilute solution, which indicate that the electronic structures of individual molecules are essentially similar and do not account for the observed differences in Φ.

In general, the AIE behaviour of crystalline Au(I) complexes can be rationalised by dense molecular packing accompanied by strong intermolecular interactions. Dense packing effectively suppresses the internal molecular motions of the luminophore and inhibits the penetration of the bulk material by molecular oxygen, thereby significantly reducing nonradiative decay pathways, particularly those associated with triplet excited states. Among the complexes, **DTE6-Hex** exhibited a Col_h LC phase at room temperature, in which molecular packing is less tightly organised than in a fully crystalline phase. Consequently, it showed the lowest Φ value in this series. Similarly, the Φ value of **DTE6-Et** was significantly lower than that of **DT6**, whereas **DTE6-H** displayed a comparable Φ value. These variations in Φ among **DT6** and the ester-functionalised DTE6-R derivatives are most plausibly attributed to differences in aggregate structure and packing density in the condensed phases, rather than to intrinsic electronic differences at the molecular level. In particular, the presence or absence of side-chain branching appears to influence intermolecular packing even in the crystalline state, with the branched side chains in **DTE6-Et** likely disrupting optimal intermolecular organisation and thereby reducing emission efficiency. The gradual red shift of the emission maximum with increasing side-chain steric bulk may similarly arise from subtle changes in intermolecular Au···Au interactions within the aggregated structures, as slight variations in the packing geometry of the trinuclear cores can influence orbital overlap and stabilise the emissive excited state, producing a bathochromic shift.

The luminescence spectra were recorded at temperatures covering distinct phase states, and representative results for **DTE6-H** and **DTE6-Hex** are shown in Fig. 8. For **DTE6-H**, the luminescence intensity decreased gradually upon heating within the crystalline phase (Fig. 8a and Fig. S17), which is consistent with the thermally activated nonradiative deactivation of the excited state. Quantitatively, a temperature increase of approximately 100 °C within the crystalline regime resulted in only a modest reduction in emission intensity (~25%), indicating that the emissive aggregated state in the crystal is relatively robust against thermal perturbation. In sharp contrast, a pronounced and discontinuous change was observed at the crystalline-to-Col_{ho} transition at 132 °C, as identified by DSC and POM. Upon entering the mesophase, the emission intensity dropped abruptly to approximately one-half of the crystalline value, accompanied by a slight broadening of the luminescence band. The mesophase of **DTE6-H** is assigned to Col_{ho}, in which long-range columnar positional order is retained while the intracolumnar packing adopts a temperature-dependent, dynamically averaged arrangement. The abrupt decrease in luminescence intensity at the crystalline-to-Col_{ho} transition therefore indicates that the emissive aggregate environment is modified primarily by reorganisation of the supramolecular packing rather than by thermal activation alone.

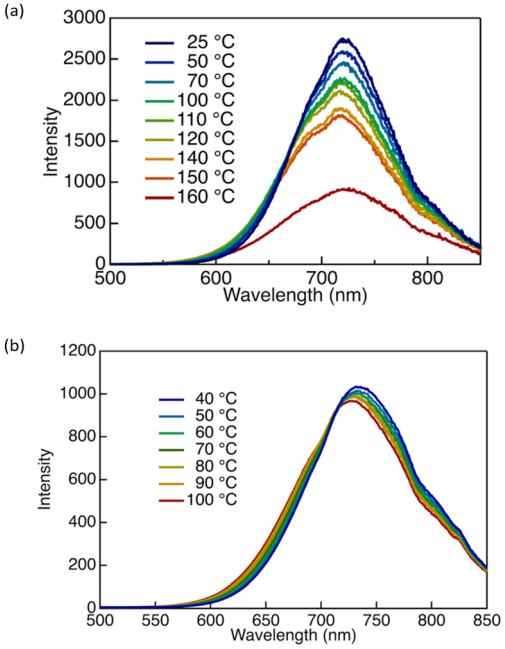

Fig. 8 Photoluminescence spectra (λ_{ex} = 300 nm) of (a) **DTE6-H** and (b) **DTE6-Hex** at various temperatures.

In contrast to **DTE6-H**, **DTE6-Hex** exhibited a distinctly different temperature-dependent luminescence behaviour that reflects its unique phase sequence. Above 35 °C, **DTE6-Hex** remained in the Col_{h2} phase up to its T_{dec} (Fig. 8b and Fig. S19). Within this high-temperature mesophase, the emission intensity was remarkably insensitive to temperature: heating from room temperature to 100 °C caused a decrease of only ~10% in luminescence intensity, despite a temperature increase of nearly 60 °C. This weak temperature dependence indicates that the emissive aggregated state formed in the Col_{h2} phase is highly stable and robust against thermally activated molecular motions. In this regime, the hexagonal columnar positional order is preserved, while intracolumnar packing is dynamically averaged, such that thermal fluctuations do not significantly perturb the emissive aggregate structure responsible for luminescence.

At cryogenic temperatures, **DTE6-Hex** displayed noticeably different photophysical behaviour (Fig. S18 and S19). At −196 °C, the emission intensity was enhanced by approximately a factor of two relative to that at room temperature and was accompanied by a blue shift of approximately 10 nm. This enhancement is consistent with the suppression of structural relaxation and nonradiative decay pathways at low temperature. Importantly, **DTE6-Hex** existed as a glass-like LC solid below −15 °C, in which long-range hexagonal columnar order is retained while molecular mobility is strongly suppressed. Within this low-temperature solid regime, the luminescence intensity showed only minimal variation: even upon heating from −196 °C to approximately −20 °C (a temperature change of nearly 180 °C), the emission intensity decreased by only ~10%. This observation demonstrates that the emissive aggregate structure in the LC-like solid state is highly resistant to thermal perturbation.

In sharp contrast, the emission intensity considerably decreased in the intermediate temperature range between approximately −15 °C and 35 °C, corresponding to the Col_{h1} phase. Within this relatively narrow temperature window of ~40 °C, the photoluminescence intensity decreased rapidly by ~50%. In this phase, long-range columnar positional order is preserved but localised packing motifs—associated with partially immobilised or correlated alkyl chain domains—became increasingly sensitive to thermal activation. The strong temperature dependence of the emission intensity in this regime indicates that the emissive aggregated species are particularly susceptible to subtle changes in local packing coherence, even though the overall columnar lattice remains intact.

These results demonstrate that the temperature dependence of the luminescence of **DTE6-Hex** is governed primarily by phase structure rather than by thermal energy alone. Both the LC-like solid below −15 °C and fully disordered Col_{h2} phase above 35 °C exhibit highly temperature-insensitive emission, whereas the intermediate Col_{h1} phase displays a pronounced decrease in emission intensity owing to the progressive disruption of residual local order by thermal activation. This phase-dependent modulation of thermal sensitivity highlights the critical role of hierarchical aggregation—combining long-range columnar order with temperature-sensitive short-range correlations—in controlling the RTP behaviour of **DTE6-Hex.**

Linearly polarised luminescence

DTE6-Hex exhibits an LC phase at room temperature; therefore, to elucidate its optical anisotropy and molecular orientation, linearly polarised luminescence (LPL) measurements were performed. A linear polariser was placed between the sample and detector of the spectrometer. The sample was sandwiched between two quartz plates, and unidirectional shear stress was applied to induce macroscopic alignment of the LC domains. The formation of a homogeneously aligned state was preliminarily confirmed by POM (Fig. S20).

The emission intensity showed a strong dependence on the relative orientation between the optical axis of the polariser and shear alignment direction (Fig. 9). The emission intensity was at a maximum when the optical axis was parallel to the shear direction ($\theta = 0^\circ$). As θ increased, the emission intensity gradually decreased and reached a minimum when the two directions were perpendicular ($\theta = 90^\circ$). Such angular dependence is characteristic of linearly polarised emission, for which the emission intensity is proportional to $\cos^2\theta$.[70] Indeed, fitting the experimental data to a $\cos^2\theta$-type function reproduced the observed angular modulation very well (Fig. 8b). This result confirms that the observed emission anisotropy originates from LPL resulting from shear-induced uniaxial alignment of the Col_h columns.

Based on these measurements, the degree of polarisation (P) was calculated using the following equation:

$$P = \frac{I_{\parallel} - I_{\perp}}{I_{\parallel} + I_{\perp}} \quad (1)$$

where $I_{\parallel}$ and $I_{\perp}$ are the emission intensities measured with the optical axis of polariser parallel and perpendicular to the shear alignment direction, respectively. The P of **DTE6-Hex** was 0.72, indicating highly efficient LPL. This polarised emission is attributed mainly to shear-induced macroscopic alignment of the columnar LC domains, which preferentially orients the emissive transition dipole moments along a single direction. The emission of trinuclear Au(I) complexes originates from aurophilic interactions.[18] Our previous study demonstrated that the emission transition dipole moment of aggregated trinuclear Au(I) complexes is preferentially oriented along the direction of aurophilic interactions.[9] This implies that, in such columnar assemblies, the transition dipole moments are aligned predominantly along the column axis. Consequently, uniaxial ordering of the columns leads to anisotropic emission, with the emission intensity reaching a maximum when the optical axis is parallel to the column alignment direction ($\theta = 0^\circ$) and a minimum when it is perpendicular ($\theta = 90^\circ$). The high P reflects strong orientational order in the emitting state.

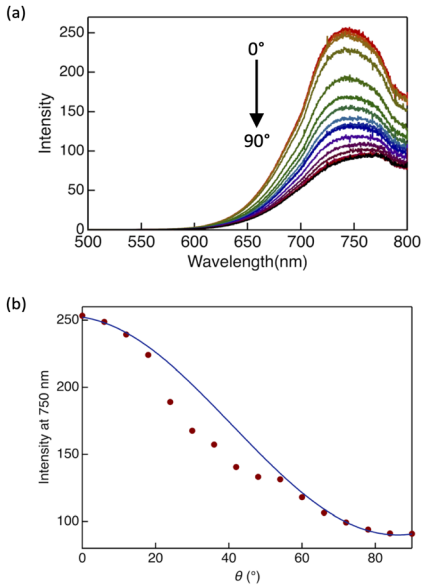

Fig. 9 (a) Polarised luminescence spectra of **DTE6-Hex** in the disordered hexagonal columnar (Col_h) phase at room temperature. The emission spectra were measured by varying the angle θ between the optical axis of the polariser and shear alignment direction of the liquid crystalline sample from 0° to 90°. (b) Emission intensity at 750 nm as a function of θ (red circles). The blue solid line represents the fitting curve obtained using a $\cos^2\theta$-type function, highlighting the characteristic angular dependence of linearly polarised luminescence.

Conclusions

We developed a new series of pyrazole-based cyclic trinuclear Au(I) complexes (DTE6-R) with flexible ester-linked alkyl side chains to systematically investigate how linker chemistry and side-chain architecture cooperatively govern LC behaviour, thermal stability, and photophysical properties. All DTE6-R derivatives self-assembled into the Col_h mesophase. Increasing the degree of sidechain branching effectively suppressed crystallisation and lowered the melting temperature, while incorporating

an ester linkage markedly stabilised the columnar LC phase at elevated temperatures. This synergistic effect dramatically expanded the LC temperature window relative to that of the reference complex **DT6**. Notably, **DTE6-Hex** exhibited a stable room-temperature Col_h phase and exceptionally broad mesophase range, with no detectable transition to an isotropic liquid prior to thermal decomposition.

Despite these pronounced differences in phase behaviour, the photophysical characteristics of the complexes in the condensed state were remarkably robust across the series. All complexes exhibited AIE and ambient-stable red-to-NIR phosphorescence, indicating that the emissive excited state is primarily dictated by a characteristic supramolecular aggregation motif rather than by a specific alkyl substituent or macroscopic phase state. In contrast, the photoluminescence quantum yield showed a clear dependence on molecular packing density, gradually decreasing with increasing side-chain length. Importantly, the practical functionality of these materials was demonstrated by their macroscopic optical anisotropy: shear-aligned **DTE6-Hex** displayed highly linearly polarised NIR emission with a high degree of polarisation. Materials exhibiting such pronounced LPL behaviour are therefore promising candidates for polarised light sources and hold significant potential for applications in anti-counterfeiting technologies and information encoding.

This study establishes that ester linker incorporation and branched side-chain engineering play distinct yet complementary roles, enabling independent control over the lower and upper temperature boundaries of the LC phase. This dual-parameter design strategy gives rise to an unusually broad LC mesophase window that is unprecedented for luminescent cyclic trinuclear Au(I) complexes. The present findings provide a versatile molecular framework for the design of thermally robust, RTP-active, and NIR-emissive LC materials and open new avenues toward soft photonic and optoelectronic applications based on metal-containing supramolecular systems. Importantly, this work demonstrates that the liquid crystallinity and luminescence of cyclic trinuclear Au(I) complexes can be decoupled and independently engineered—a long-standing challenge in metal-containing soft luminescent materials.

Experimental

Materials

The Au(I) complex **DT6** was synthesised according to a previously reported procedure.[13] The DTE6-R (R = H, Et, or Hex) complexes were prepared from ethyl diacetoacetate in four synthetic steps, as outlined in Scheme S1. All solvents and reagents were of reagent grade and used as received unless otherwise stated. ^{1}H and ^{13}C NMR spectra were obtained using a JEOL ECS 400 MHz NMR spectrometer operated at 395.884 MHz for ^{1}H and 99.545 MHz for ^{13}C. Chemical shifts are reported in parts per million (ppm), using the residual proton or carbon in the NMR solvent. FTIR spectra were recorded on a JASCO FT/IR-610 spectrometer using the KBr disk method and are reported in wavenumbers (cm^{-1}). ESI-MS measurements were carried out using a Bruker micrOTOF II mass spectrometer. Elemental analyses were performed using a J-Science Micro Corder JM10 analyser.

Typical procedure for the synthesis of Au(I) complexes with ester-linked alkyl side chains

Synthesis of DTE6-H. A methanolic solution of KOH (1 mol L^{-1}, 0.40 mL) was added dropwise to a stirred solution of compound 3H (83 mg, 0.37 mmol) and (tht)AuCl (80 mg, 0.25 mmol) in acetone (15 mL). After stirring for 10 min at room temperature (25 °C), the resulting precipitate was collected by filtration and washed with acetone. The crude product was purified by silica gel column chromatography (eluent: CH_2Cl_2/triethylamine = 30/1), followed by recrystallisation from a 1 : 1 mixture of CH_2Cl_2 and acetone to afford colourless crystals (64 mg, 0.051 mmol, 61% yield). mp 131.7–133.5 °C (from a mixture of CH_2Cl_2 and acetone). Found: C, 34.20; H, 4.56; N, 6.78; Ash, 46.7; M^+, 1260.40. Calc. for $C_{36}H_{57}Au_3N_6O_6$: C, 34.30; H, 4.56; N, 6.67%; M^+, 1260.33. ν/cm^{-1} 2959, 2930, 2873, 1706, 1522, 1425, 1290, 1120, 780. δ_H (400 MHz; $CDCl_3$) 4.16 (2H, t, J = 6.8 Hz, $COOC\underline{H}_2C_5H_{11}$), 2.16 (6H, s, pyr-$C\underline{H}_3$), 1.70 (2H, quint, J = 7.1 Hz, $COOCH_2C\underline{H}_2C_4H_9$), 1.43–1.32 (6H, m, $COOC_2H_4C_3\underline{H}_6CH_3$), 0.92 (3H, t, J = 6.8 Hz, $COOC_5H_{10}C\underline{H}_3$). δ_C (100 MHz; $CDCl_3$,) 164.0, 150.9, 77.3, 77.0, 76.7, 63.8, 28.7, 25.8, 22.6, 14.2, 14.0.

Synthesis of DTE6-Et and DTE6-Hex. These compounds were synthesised according to the above procedure. **DTE6-Et** was obtained in 26% yield as a white solid and **DTE6-Hex** in 29% yield as a white viscous material.

DTE6-Et. mp 98.3–100.2 °C (from a mixture of CH_2Cl_2 and acetone). Found: C, 37.83; H, 5.12; N, 6.26; Ash, 43.2; M^+, 1344.84. Calc. for $C_{42}H_{69}Au_3N_6O_6$: C, 37.51; H, 5.17; N, 6.25%; M^+, 1344.43. ν/cm^{-1} 2957, 2929, 2875, 1712, 1520, 1425, 1383, 1287, 1167, 1119, 770. δ_H (400 MHz; $CDCl_3$) 4.13 (6H, octet, J = 5.4 Hz, $COOCH_2$ $CH(C_2H_5)C_4H_9$), 2.50 (18H, s, pyr-CH_3), 1.67–1.51 (3H, m, $COOCH_2CH(C_2H_5)C_4H_9$), 1.47–1.28 (24H, m, $COOCH_2CH(C\underline{H}_2CH_3)C_3\underline{H}_6CH_3$), 0.95–0.87 (18H, m, $COOCH_2$-$CH(CH_2C\underline{H}_3)C_3H_6C\underline{H}_3$). δ_C (100 MHz; $CDCl_3$): 164.2, 151.3, 109.0, 77.3, 77.2, 77.0, 76.7, 66.0, 38.8, 30.4, 28.9, 23.8, 23.0, 14.3, 14.1, 10.9.

DTE6-Hex. mp −15.1 to −11.2 °C (from a mixture of CH_2Cl_2 and acetone). Found: C, 42.60; H, 5.88; N, 5.58; Ash 38.7; M^+, 1513.87. Calc. for $C_{54}H_{93}Au_3N_6O_6$: C, 42.86; H, 6.19; N, 5.55%; Ash, 39.05; M^+, 1513.27. ν/cm^{-1} 2956, 2927, 2858, 1706, 1522, 1424, 1376, 1291, 1169, 1110, 1037, 726. δ_H (400 MHz; $CDCl_3$) 4.12 (2H, d, J = 5.4 Hz, $COOC\underline{H}_2CH(C_6H_{13})C_4H_9$), 2.24 (6H, s, pyr-$C\underline{H}_3$), 1.72 (1H, m, $COOCH_2C\underline{H}(C_6H_{13})C_4H_9$), 1.33–1.29 (16H, m, $COOCH_2CH$-$(C_5\underline{H}_{10}CH_3)C_3\underline{H}_6CH_3$), 0.93–0.87 (6H, m, $COOCH_2CH(C_5H_{10}$-$C\underline{H}_3)C_3H_6C\underline{H}_3$). δ_C (100 MHz; $CDCl_3$) 164.3, 151.5, 109.2, 66.6, 37.5, 32.0, 31.4, 31.1, 29.8, 28.9, 26.8, 23.2, 22.8, 14.6, 14.2.

Computation

All calculations were performed using DFT, as implemented in the Gaussian 16 program package (Revision C.01).[71] To reduce

computational cost, simplified model complexes (DT1 and DTE1, Fig. S21) were employed. Geometry optimisation of monomeric species was carried out using the B3LYP hybrid functional with the 6-311+G(d,p) basis set for C, H, N, and O atoms and SDD basis set for Au atoms. Dimer calculations were performed using the CAM-B3LYP-D3(BJ) functional with the same basis sets. Optimised geometries were confirmed as true minima by vibrational frequency analysis. Vertical excitation energies and oscillator strengths for the ten lowest electronic transitions were calculated using TD-DFT based on the optimised ground-state geometries.

Powder X-ray diffraction

VT-PXRD measurements were performed using a Malvern Panalytical Aeris powder diffractometer equipped with a PIXcel1D (Medipix3-based) solid-state line detector. Cu Kα radiation (λ = 1.5406 Å) was used as the X-ray source. Data were collected in the 2θ range of 4–50° with a step size of 0.1086° and a scan speed of 0.3951° s^{-1} in continuous scan mode. Temperature control was achieved using an integrated heating stage, and samples were equilibrated at each temperature for at least 5 min prior to data acquisition.

Small-angle X-ray scattering

SAXS measurements were performed at the BL40B2 beamline of SPring-8 (Hyogo, Japan) using monochromatic X-ray radiation with a wavelength of λ = 1.0 Å. Measurements were carried out at controlled temperatures of −25, 0, 15, and 40 °C using a temperature-regulated sample stage. Samples were equilibrated at each temperature prior to data acquisition. Scattering profiles were recorded as a function of the magnitude of the scattering vector, q, defined as $q = (4\pi/\lambda) \sin \theta$, where 2θ represents the scattering angle.

Thermodynamic properties

Phase transitions were observed by POM using an Olympus BX51 fluorescence microscope equipped with a temperature-controlled stage (Instec HCS302 with mK1000 controller). TGA and differential thermal analysis were carried out using a Shimadzu DTG-60AH analyser at a heating rate of 5.0 °C min^{-1}. DSC measurements were conducted using an SII X-DSC7000 differential scanning calorimeter at heating and cooling rates of 2.0 °C min^{-1}. At least three DSC scans were recorded to ensure reproducibility.

Photophysical properties

UV-vis absorption spectra were recorded on a Jasco V-500 spectrophotometer. Steady-state photoluminescence spectra were measured using a Hitachi F-7000 fluorescence spectrometer. For condensed-phase measurements, samples were sandwiched between two quartz plates and placed on a homemade temperature-controlled stage. Low-temperature photoluminescence measurements were performed using a cryostat system (Oxford Instruments, OptistatDN-V) with liquid nitrogen as the cryogen.

Photoluminescence quantum yields (Φ) were determined using a calibrated integrating sphere system (Hitachi). Photoluminescence decay profiles were recorded on a fluorescence lifetime spectrometer (Hamamatsu, Quantaurus-Tau C1136-21) with an excitation wavelength of 280 nm.

Author contributions

Conceptualisation, O. T.; formal analysis, T. N., A. S., K. Y., A. R., K. M., and P. G.; funding acquisition, O. T. and K. M.; investigation, T. N., A. S., K. Y., K. K., and K. M.; methodology, T. N., A. S., K. Y., K. K., and K. M.; visualisation, O. T. and K. M.; writing – original draft, T. N., A. S., and O. T.; writing – review & editing, O. T., A. R., K. M., and P. G.

Conflicts of interest

There are no conflicts to declare.

Data availability

The supporting data has been provided as part of the supplementary information (SI). Supplementary information: Tables S1–S4; NMR spectra; thermal properties; POM images; PXRD; SAXS; SCXRD; luminescence properties; DFT calculation and further experimental details. See DOI: https://doi.org/10.1039/d6tc00570e.

Acknowledgements

This work was supported by the Japan Society for the Promotion of Science (JSPS) KAKENHI (24K01561 and 24K21799 to O. T. and 25K18089 to K. M.), Japan Science and Technology Agency (JST) LOTUS programme (25152949), JST Japan–ASEAN Science, Technology and Innovation (STI) Program for Young Researchers (Y2025L1015007), and Japan–India Science Cooperative Program between the JSPS and Department of Science & Technology (DST), India (JPJSBP120217716). Synchrotron radiation experiments were performed at the BL40B2 beamline of SPring-8 (Hyogo, Japan) with the approval of the Japan Synchrotron Radiation Research Institute (Proposal No. 2023A1071 and 2024A1377).

Notes and references

1 H. Sasabe and J. Kido, *J. Mater. Chem. C*, 2013, **1**, 1699–1707.
2 H. Sasabe and J. Kido, *Eur. J. Org. Chem.*, 2013, 7653–7663.
3 M.-C. Tang, M.-Y. Chan and V. W.-W. Yam, *Chem. Rev.*, 2021, **121**, 7249–7279.
4 M. Jin and H. Ito, *J. Photochem. Photobiol., C*, 2022, **51**, 100478.
5 C. Zong, L. R. Zheng, W. He, X. Ren, C. Jiang and L. Lu, *Anal. Chem.*, 2014, **86**, 1687–1692.

6 M. Rosental, R. N. Coldman, A. J. Moro, I. Angurell, R. M. Gomila, A. Frontera, J. C. Lima and L. Rodríguez, *Molecules*, 2021, **26**, 2444.
7 H. Schmidbaur and A. Schier, *Chem. Soc. Rev.*, 2008, **37**, 1931–1951.
8 H. Schmidbaur and A. Schier, *Chem. Soc. Rev.*, 2012, **41**, 370–412.
9 A. Ando, K. Ozaki, U. Shiina, E. Nagao, K. Hisano, K. Kamada and O. Tsutsumi, *Aggregate*, 2022, **3**, e125.
10 S. Pawledzio, M. Malinska, F. Kleemiss, S. Grabowsky and K. Woźniak, *Inorg. Chem.*, 2022, **61**, 4235–4239.
11 V. W.-W. Yam, V. K.-M. Au and S. Y.-L. Leung, *Chem. Rev.*, 2015, **115**, 7589–7728.
12 J. Zheng, Z. Lu, K. Wu, G.-H. Ning and D. Li, *Chem. Rev.*, 2020, **120**, 9675–9742.
13 H. Schmidbaur and H. G. Raubenheimer, *Angew. Chem., Int. Ed.*, 2020, **59**, 14748–14771.
14 G. Yang and R. G. Raptis, *Inorg. Chem.*, 2003, **42**, 261–263.
15 Y.-X. Chen, H. Yu, L. Wu, Y.-J. Tong, J. Xu, H. Pang, C. Wu, T. Tian and G. Ouyang, *Nat. Commun.*, 2024, **15**, 7356.
16 L. D. Earl, J. K. Nagle and M. O. Wolf, *Inorg. Chem.*, 2014, **53**, 7106–7117.
17 J. Mei, N. L. C. Leung, R. T. K. Kwok, J. W. Y. Lam and B. Z. Tang, *Chem. Rev.*, 2015, **115**, 11718–11940.
18 Y. Kuroda, M. Tamaru, H. Nakasato, K. Nakamura, M. Nakata, K. Hisano, K. Fujisawa and O. Tsutsumi, *Commun. Chem.*, 2020, **3**, 139.
19 K. Fujisawa, S. Yamada, Y. Yanagi, Y. Yoshioka, A. Kiyohara and O. Tsutsumi, *Sci. Rep.*, 2015, **5**, 7934.
20 Y. Tian, Z.-Y. Wang, S.-Q. Zang, D. Li and T. C. W. Mak, *Dalton Trans.*, 2019, **48**, 2275–2279.
21 O. Tsutsumi, M. Tamaru, H. Nakasato, S. Shimai, S. Panthai, Y. Kuroda, K. Yamaguchi, K. Fujisawa and K. Hisano, *Molecules*, 2019, **24**, 4606.
22 Y. Hong, J. W. Y. Lam and B. Z. Tang, *Chem. Commun.*, 2009, 4332–4353.
23 X.-Y. Zhai and L. Zhao, *Nat. Commun.*, 2025, **16**, 405.
24 W. Ni, M. Li, J. Zheng, S.-Z. Zhan, Y.-M. Qiu, S. W. Ng and D. Li, *Angew. Chem., Int. Ed.*, 2013, **52**, 13472–13476.
25 C. Yang, M. Messerschmidt, P. Coppens and M. A. Omary, *Inorg. Chem.*, 2006, **45**, 6592–6594.
26 J.-B. Li, H.-W. Liu, T. Fu, R. Wang, X.-B. Zhang and W. Tan, *Trends Chem.*, 2019, **1**, 224–234.
27 W. Liang, S. He and S. Wu, *Adv. NanoBiomed Res.*, 2022, **2**, 2200087.
28 E. A. Owens, M. Henary, G. El Fakhri and H. S. Choi, *Acc. Chem. Res.*, 2016, **49**, 1731–1740.
29 Q. Fu, C. Wei, X. Yang, M. Wang and J. Song, *Aggregate*, 2025, **6**, e652.
30 C. Liu, T. Tian, Y. Shi, M. Li, L. Hong, J. Zhou, J. Liu, Y. Zhong, X. Wang, Z. Wang, X. Bai, L. Wang, C. Li and Z. Wu, *Aggregate*, 2025, **6**, e666.
31 A. Minotto, P. A. Haigh, G. Łukasiewicz, E. Lunedei, D. T. Gryko, I. Darwazeh and F. Cacialli, *Light: Sci. Appl.*, 2020, **9**, 70.
32 Z. Chen, H. Zhang, D. Wen, W. Wu, Q. Zeng, S. Chen and W.-Y. Wong, *Chem. Sci.*, 2020, **11**, 2342–2349.
33 C. T. Jackson, S. Jeong, G. F. Dorlhiac and M. P. Landry, *iScience*, 2021, **24**, 102156.
34 P. L. dos Santos, P. Stachelek, Y. Takeda and P. Pander, *Mater. Chem. Front.*, 2024, **8**, 1731–1766.
35 M. Ibrahim-Ouali and F. Dumur, *Molecules*, 2019, **24**, 1412.
36 C.-L. Ho, H. Li and W.-Y. Wong, *J. Organomet. Chem.*, 2014, **751**, 261–285.
37 H.-H. Cho, S. Gorgon, G. Londi, S. Giannini, C. Cho, P. Ghosh, C. Tonnelé, D. Casanova, Y. Olivier, T. K. Baikie, F. Li, D. Beljonne, N. C. Greenham, R. H. Friend and E. W. Evans, *Nat. Photonics*, 2024, **18**, 905–912.
38 X. Wang, F. Ding, T. Jia, F. Li, X. Ding, R. Deng, K. Lin, Y. Yang, W. Wu, D. Xia and G. Chen, *Nat. Commun.*, 2024, **15**, 2157.
39 Y. Ren, Y. Zhang, H. Su, Y. Zhao, W. Yan, W. Dai, L. Zhu, T. Wang, J. Shi, J. Zhi, B. Tong, P. Sun, Z. Cai and Y. Dong, *Nat. Commun.*, 2025, **16**, 11120.
40 C. Schweitzer and R. Schmidt, *Chem. Rev.*, 2003, **103**, 1685–1758.
41 M. A. Filatov, S. Baluschev and K. Landfester, *Chem. Soc. Rev.*, 2016, **45**, 4668–4689.
42 F. Xiao, H. Gao, Y. Lei, W. Dai, M. Liu, X. Zheng, Z. Cai, X. Huang, H. Wu and D. Ding, *Nat. Commun.*, 2022, **13**, 186.
43 B. Ding, X. Ma and H. Tian, *Acc. Mater. Res.*, 2023, **4**, 827–838.
44 Y. Wang, J. Shi, J. Chen, W. Zhu and E. Baranoff, *J. Mater. Chem. C*, 2015, **3**, 7993–8005.
45 C. Cuerva, M. Cano and C. Lodeiro, *Chem. Rev.*, 2021, **121**, 12966–13010.
46 A. A. Knyazev, A. S. Krupin, B. Heinrich, B. Donnio and Y. G. Galyametdinov, *Dyes Pigm.*, 2018, **148**, 492–500.
47 K. Minoura, Y. Akama, J. Morita, T. Yasuda, T. Kato and T. Shimomura, *J. Appl. Phys.*, 2009, **105**, 113513.
48 D. Fu, S. Liu, X. Yang, Z. Chen and S. H. Liu, *Aggregate*, 2025, **6**, e70079.
49 T. Wöhrle, I. Wurzbach, J. Kirres, A. Kostidou, N. Kapernaum, J. Litterscheidt, J. C. Haenle, P. Staffeld, A. Baro, F. Giesselmann and S. Laschat, *Chem. Rev.*, 2016, **116**, 1139–1241.
50 S. Furumi, D. Janietz, M. Kidowaki, M. Nakagawa, S. Morino, J. Stumpe and K. Ichimura, *Chem. Mater.*, 2001, **13**, 1434–1437.
51 R. De, S. Sharma, S. Sengupta and S. K. Pal, *Chem. Rec.*, 2022, **22**, e202200056.
52 S. J. Kim, S. H. Kang, K.-M. Park, H. Kim, W.-C. Zin, M.-G. Choi and K. Kim, *Chem. Mater.*, 1998, **10**, 1889–1893.
53 J. Cored, O. Crespo, J. L. Serrano, A. Elduque and R. Giménez, *Inorg. Chem.*, 2018, **57**, 12632–12640.
54 J. Barberá, A. Elduque, R. Giménez, L. A. Oro and J. L. Serrano, *Angew. Chem., Int. Ed. Engl.*, 1996, **35**, 2832–2835.
55 E. Beltrán, J. Barberá, J. L. Serrano, A. Elduque and R. Giménez, *Eur. J. Inorg. Chem.*, 2014, 1165–1173.
56 M. C. Torralba, P. Ovejero, M. J. Mayoral, M. Cano, J. A. Campo, J. V. Heras, E. Pinilla and M. R. Torres, *Helv. Chim. Acta*, 2004, **87**, 250–263.
57 E. De Domingo, G. García, E. Tritto, B. Donnio, A. Shah, D. P. Singh and S. Coco, *J. Mater. Chem. C*, 2025, **13**, 8563–8570.
58 M. Bardají, *Inorganics*, 2014, **2**, 433–454.

59 Y. Kuroda, S. Nakamura, K. Srinivas, A. Sathyanarayana, G. Prabusankar, K. Hisano and O. Tsutsumi, *Crystals*, 2019, **9**, 227.
60 S. Yamada, S. Yamaguchi and O. Tsutsumi, *J. Mater. Chem. C*, 2017, **5**, 7977–7984.
61 C. Hansch, A. Leo and R. W. Taft, *Chem. Rev.*, 1991, **91**, 165–195.
62 S.-H. Cha, K.-H. Kim, J.-U. Kim, W.-K. Lee and J.-C. Lee, *J. Phys. Chem. C*, 2008, **112**, 13862–13868.
63 E. Fontes, P. A. Heiney and W. H. De Jeu, *Phys. Rev. Lett.*, 1988, **61**, 1202–1205.
64 J. Simmerer, B. Glüsen, W. Paulus, A. Kettner, P. Schuhmacher, D. Adam, K.-H. Etzbach, K. Siemensmeyer, J. H. Wendorff, H. Ringsdorf and D. Haarer, *Adv. Mater.*, 1996, **8**, 815–819.
65 W. Pisula, M. Kastler, D. Wasserfallen, M. Mondeshki, J. Piris, I. Schnell and K. Müllen, *Chem. Mater.*, 2006, **18**, 3634–3640.
66 S. Kumar, D. S. S. Rao and S. K. Prasad, *J. Mater. Chem.*, 1999, **9**, 2751–2754.
67 S. Sergeyev, E. Pouzet, O. Debever, J. Levin, J. Gierschner, J. Cornil, R. Gómez Aspe and Y. H. Geerts, *J. Mater. Chem.*, 2007, **17**, 1777–1784.
68 S. K. Prasad, D. S. S. Rao, S. Chandrasekhar and S. Kumar, *Mol. Cryst. Liq. Cryst.*, 2003, **396**, 121–139.
69 C. Roche, H.-J. Sun, P. Leowanawat, F. Araoka, B. E. Partridge, M. Peterca, D. A. Wilson, M. E. Prendergast, P. A. Heiney, R. Graf, H. W. Spiess, X. Zeng, G. Ungar and V. Percec, *Nat. Chem.*, 2016, **8**, 80–89.
70 J. R. Lakowicz, *Principles of Fluorescence Spectroscopy*, Springer, Boston, 3rd edn, 2006, ch. 10, pp. 353–381.
71 M. J. Frisch, G. W. Trucks, H. B. Schlegel, G. E. Scuseria, M. A. Robb, J. R. Cheeseman, G. Scalmani, V. Barone, G. A. Petersson, H. Nakatsuji, X. Li, M. Caricato, A. V. Marenich, J. Bloino, B. G. Janesko, R. Gomperts, B. Mennucci, H. P. Hratchian, J. V. Ortiz, A. F. Izmaylov, J. L. Sonnenberg, D. Williams-Young, F. Ding, F. Lipparini, F. Egidi, J. Goings, B. Peng, A. Petrone, T. Henderson, D. Ranasinghe, V. G. Zakrzewski, J. Gao, N. Rega, G. Zheng, W. Liang, M. Hada, M. Ehara, K. Toyota, R. Fukuda, J. Hasegawa, M. Ishida, T. Nakajima, Y. Honda, O. Kitao, H. Nakai, T. Vreven, K. Throssell, J. A. Montgomery Jr, J. E. Peralta, F. Ogliaro, M. J. Bearpark, J. J. Heyd, E. N. Brothers, K. N. Kudin, V. N. Staroverov, T. A. Keith, R. Kobayashi, J. Normand, K. Raghavachari, A. P. Rendell, J. C. Burant, S. S. Iyengar, J. Tomasi, M. Cossi, J. M. Millam, M. Klene, C. Adamo, R. Cammi, J. W. Ochterski, R. L. Martin, K. Morokuma, O. Farkas, J. B. Foresman and D. J. Fox, *Gaussian 16, Revision C.01*, Gaussian Inc., Wallingford CT, 2019.